Research Square

Preprints are preliminary reports that have not undergone peer review.
They should not be considered conclusive, used to inform clinical practice,
or referenced by the media as validated information.

Membrane destabilization is a critical step in antimicrobial peptide effectivity

Logan Hartmann
Carnegie Mellon University
Austin Leong
Carnegie Mellon University
Rohan Parasnis
Carnegie Mellon University
Ashley Hackney
Carnegie Mellon University
Anika Bhawalkar
Carnegie Mellon University
Danny Weng
Carnegie Mellon University
Weicheng Gao
Carnegie Mellon University
Vicky Yan
Carnegie Mellon University
Zoe Hausner
Carnegie Mellon University
Meitung Chen
Carnegie Mellon University
Lucy Knox
Carnegie Mellon University
Jad Jaber
University of Pittsburgh
Jessie Klousnitzer
University of Pittsburgh
Wenyu Xiang
University of Pittsburgh
Berthony Deslouches
University of Pittsburgh
Stephanie Tristram-Nagle
stn@cmu.edu

Carnegie Mellon University

Research Article

Keywords: X-ray diffuse scattering, antimicrobial peptides, antimicrobial resistance, circular dichroism

Posted Date: August 19th, 2026

DOI: https://doi.org/10.21203/rs.3.rs-10617120/v1

License: This work is licensed under a Creative Commons Attribution 4.0 International License.
Read Full License

Additional Declarations: No competing interests reported.

Abstract

This work examined biophysical properties of a matched pair of antimicrobial peptides (AMPs), **RT9** (VRRW VRRV WRWV RRVW RR) and **KT9** (VKKW VKKV WKWV KKVW KK), two 18-mers that contain only four types of amino acids: valine (V) and tryptophan (W) as the hydrophobic, and lysine (K) or arginine (R) as the cationic amino acids. Microbiological testing revealed that KT9 was more effective at killing both Gram-negative G(-) and Gram-positive G(+) bacteria, but that RT9 was more toxic to red blood cells. Circular dichroism (CD) spectroscopy showed slightly higher helical content of RT9 vs KT9 in three different lipid model membranes (LMMs) that mimic G(-), G(+) and eukaryotic (Euk33) membranes, but that alpha-helical content was much lower than beta-sheet and random coil content in both AMPs. X-ray scattering data on hydrated, oriented lipid/AMP films collected at the CHESS synchrotron showed a decrease in membrane rigidity as both AMPs were added to the three LMMs, and a decrease in lipid chain order except for RT9 in Euk33 LMM. Electron density profiles showed that KT9 locates in the headgroup of both G(-) and G(+) LMMs, while RT9 locates in the hydrocarbon interior. Both AMPs locate in the chain region in Euk33 LMMs. Small-angle X-ray scattering quantitated conversion of unilamellar to multilamellar vesicles, which indicates that lipid membrane fusion had occurred. The fusion, or membrane destabilization, was greater for KT9 in bacterial LMMs, but greater for RT9 in Euk33 LMMs, highlighting a correlation of membrane fusion with bacterial killing efficacy or eukaryotic toxicity.

Key points

● KT9 is more effective than RT9 at killing bacteria and is less toxic.

● KT9 causes more fusion than RT9 of bacterial ULVs to MLVs, and less for eukaryotic.

● KT9 and RT9 locate differently in bacterial LMMs.

Introduction

Bacterial resistance to antibiotics represents one of the most severe public health threats in today's society, with recent projections estimating that 50 million people will be at risk of severe illness or death in the next 25 years (CDC 2025). Consequently, there is an urgent need for feasible alternatives to mitigate this dangerously rising mortality; antimicrobial peptides have emerged as prime candidates. Many AMPs are amphipathic, meaning they are composed of both hydrophobic and hydrophilic parts. After binding to an amphipathic bilayer, AMPs can kill bacteria by first introducing membrane instability, which is sometimes followed by an intracellular lethal mechanism (Hale and Hancock 2007). Membrane perturbations include toroidal pores ((Hallock et al. 2003; Matsuzaki et al. 1997), barrel-stave pores (He et al. 1996), interfacial activity (Rathinakumar and Wimley 2008), a carpet model (Shai 1999), bilayer thinning (Aisenbrey 2019; Chen et al. 2003; Heinrich et al. 2020), segregation of charged lipids (Epand and Epand 2009), and aggregation (Wu et al. 2010). As a result, AMPs have become one center of study in creating therapeutic solutions to aid in slowing down the ongoing antibiotic resistance crisis.

In this study, we characterize the secondary structure and membrane dynamics of a matched set of T9 AMPs, both 18-mers, which contain only four types of amino acid: lysine or arginine (cationic), along with valine and tryptophan (hydrophobic). X-ray diffuse scattering (XDS) is used to analyze the localization of the peptide and its effect on membrane structure, as well as its impact on membrane rigidity and chain ordering. Unilamellar vesicle fusion into multilamellar vesicles is quantitated by small-angle X-ray scattering (SAXS) to gain insight into the destabilization of the membrane. Circular dichroism (CD) is used to quantitate the secondary structure composition. These biophysical properties are compared to the T9 peptides' effects on bacterial killing and eukaryotic cell toxicity. The helical wheel representations are shown in Fig.1.

Materials and Methods

Bacterial killing efficacy and toxicity to eukaryotic cells

AMPs were tested against bacterial clinical isolates provided by the Center for Disease Control and Prevention to determine minimum inhibitory concentrations (MICs). Toxicity to mammalian cells was examined by the ability of AMPs to induce direct lysis of human red blood cells (RBC; Vitalant, Pittsburgh, PA, USA) in phosphate buffered saline (PBS), which is indicated by the release of hemoglobin as previously described (Mitra et al. 2023). Briefly, to examine antibacterial activity, we used minor modifications of a standard growth inhibition assay endorsed by the Clinical and Laboratory Standards Institute (Deslouches et al. 2013). Bacteria (~ 10^6 colony-forming units (CFU)/mL) were incubated with each of the indicated peptides, which were serially diluted 2-fold in Mueller Hinton Broth 2 in a 96-well plate. The peptide-bacteria mixture was incubated at 37^{o}C using a plate reader (Agilent, Santa Clara, CA, USA) to detect bacterial growth every hour for 24h. We define minimum inhibitory concentration (MIC) as the minimum peptide concentration that completely prevents bacterial growth, demonstrated by a flat (horizontal line) growth curve as a function of hourly determinations for 18 h at A570, in duplicate or triplicate. For the RBC lysis assay, the isolated RBCs were resuspended in PBS at a concentration of 5%. The peptides were serially diluted twofold in 100 µL of PBS before adding 100 µL of 5% RBC to a final dilution of 2.5% RBC to ensure that the A570 of hemoglobin did not saturate the plate reader. In parallel, the RBCs were osmotically lysed with water at increasing concentrations to generate a standard curve of RBC lysis. Three technicians independently conducted experiments to ensure reproducibility.

Circular Dichroism

Unilamellar vesicles (ULVs) of ~ 600 Å diameter (Hackney et al. 2026) were prepared using an Avanti extruder (Alabaster, AL, USA). 250 µL of 20 mg/mL multilamellar lipid vesicles (MLVs) was extruded 25 times through a single Nucleopore polycarbonate filter of size 50 nm using 0.25 mL Hamilton syringes. Concentrated ULVs were added to 3 mL of 10 µmol/L (µM) peptide in 15 mmol/L (mM) PBS at pH 7 to create lipid/peptide molar ratios of 0:1–70:1. Data were collected with a JASCO 810 CD spectrometer (Easton, MD, USA) at 37 ˚C. The samples were scanned 20 times from 200 to 240 nm at 100 nm/min and

the results were averaged. OriginPro 2024 (OriginLab, Northampton, MA, USA) was used to carry out a Levenberg-Marquardt least-squares fit of the tryptophan-subtracted ellipticity traces to four secondary structural motifs representing α-helix, β-sheet, β-turn and random coil. The L-M analysis gives a percentage match of each secondary structural motif to the total sample ellipticity.

Low-angle X-ray Scattering (LAXS)

Oriented samples consisting of approximately 1800 bilayers were prepared using the “rock and roll” method (Tristram-Nagle 2007), where the substrate is rocked while the lipid in organic solvent rolls over the surface as it evaporates. The solution is plated onto a chromic acid-cleaned Si wafer (15 mm W × 30 mm L × 1 mm H) and is dried for two hours under vacuum. Upon transfer from a cold refrigerator to a well-insulated hydration chamber held at 37 ∘C, full hydration occurs through the vapor within 10 minutes. Low-angle XDS (LAXS) data from oriented, fully hydrated samples were obtained at the ID7B2 beamline at the Center for High Energy X-ray Sciences (CHEXS) at the Cornell High Energy Synchrotron Source (CHESS) (Ithaca, NY). X-ray wavelength of 0.8856 Å was used, and the sample-to-detector (S)-distance was 348 mm, beam size 0.25 mm H and 0.5 mm V, with an Eiger 16M detector. The flat silicon wafer was rotated from 0 to 5 degrees during the data collection for 10 sec at 37 °C. At full hydration, membrane fluctuations cause “lobes” of diffuse X-ray scattering data, which are quantified by measuring the falloff in lobe intensity in the lateral direction. A more gradual falloff indicates a softer membrane, while a steeper falloff indicates a more rigid membrane (higher bending modulus, K_C) (Liu and Nagle 2004; Lyatskaya et al. 2000; Zhang et al. 1994). In the last step of the fitting process, the intensity data along the entire z range are collected to provide a form factor which is used to obtain the electron density profile across the bilayer using the scattering density profile (SDP) computer program (Kučerka et al. 2008) which depends on volumes of lipid components and peptides that are fit to a model membrane.

Wide-angle X-ray Scattering (WAXS)

Oriented, hydrated lipid model membranes (LMMs) were X-rayed at 0.3 degrees grazing angle of incidence at CHESS and background was collected at -0.3 degrees. The black line between detector panels was removed by computer-stitching two background-subtracted images collected at two detector positions. While full hydration is required for LAXS, overhydration causes a dominant, isotropic water band in the WAXS at ~ 3 Å. This band was minimized by blowing a gentle stream of air into the chamber for ~ 5 minutes. Remaining water scattering was further removed via a proprietary MATLAB script which scaled a water image background intensity to the water peak and baseline of each sample. Following background and water corrections, the lipid chain-chain correlation was seen as a prominent diffuse arc projecting radially from the equator at $d \approx 4.5\,\text{Å}.$

The azimuthal integration of this correlation's intensity is used to calculate the lipid chain order parameter, S_{xray} (Mills et al. 2008).

Small-angle X-ray Scattering (SAXS)

Unilamellar vesicles (ULVs) with a diameter of ~ 600 Å were prepared following the same protocol described for CD spectroscopy. Each sample consisted of 30 µL of 8 mg/mL ULV in 15 mM PBS buffer (pH 7.0), with lipid/peptide molar ratio 30:1. Two-dimensional scattering data was collected via 10-minute scans using a Xeuss 3.0 Xenocs (Holyoke, MA, USA) SAXS/WAXS instrument at Carnegie Mellon University. The X-ray source was a Rigaku CuK rotating anode (λ ≈ 1.5418 Å) operated at 40kV x 30mA, paired with an Eiger 1M detector. A high-flux configuration was used over a scattering vector range of ~ 0.03 to 0.73$Å^{-1}$ with a sample-to-detector distance of 370 mm. The 2D patterns were azimuthally averaged to make 1D intensity profiles and 1D buffer backgrounds were subtracted. The ULV data were scaled to match the rounded ULV form factor in the mixture of ULVs and MLVs. The area under the total curve was integrated using OriginPro 2024. The scaled ULV trace was then subtracted from the total trace and the area under the total-ULV curve was integrated. Dividing the total-ULV curve area by total curve area yielded the % ULVs converted to MLVs.

Results

Minimum inhibitory concentrations and toxicity

Figure 2 shows the average Minimum Inhibitory Concentrations (MIC) for RT9 and KT9 in several species of G(+) (pink fill) and G(-) (yellow fill) bacteria. As shown in Fig. 2a, the MICs for KT9 are smaller in most cases than the MICs for RT9, indicating that the KT9 AMP is more effective at killing both G(+) and G(-) bacteria. Figure 2b shows the relative toxicity as determined by red blood cell lysis. Since the % lysis is significantly smaller for KT9 compared to RT9, that is the indication that KT9 is less toxic, even at a concentration of 32 µM, which is ~ 10 times greater than the MIC concentration for most bacterial species. Additional details regarding the bacterial species are shown in Online Resource (Fig S1).

Circular dichroism (CD) spectroscopy

In an attempt to characterize the secondary structure of the two AMPs when interacting with G(-), G(+) and Euk33 LMMs, we carried out circular dichroism (CD) spectroscopy. Figure 3 shows mean residue ellipticities (MREs) of KT9 (**a,c,e**) and RT9 (**b,d,f)** with G(-), G(+) and Euk33 LMMs. Very little helical character is visually apparent in the MRE traces. When the four main secondary structural motifs are fit to the data in Fig. 3 (**a-f**) using the Levenberg-

Marquardt (L-M) least-squares fitting algorithm, the percent composition is quantitated as shown in Fig. 3 (**g-l**). Across all AMP-ULV mixtures, helical content is usually ≤10%, while random coil and beta-

sheet dominate.

Figure 4 Kinetics of formation of secondary structure of KT9 and RT9 in G(+) LMM (30:1 lipid/peptide molar ratio) at 37 ^{o}C, MREs (**a,b**), Percent composition (**c,d**)

Since the AMPs were added to the ULVs between 0–2 days before CD data were collected, a kinetic study was conducted to test for a time dependence of secondary structure formation, as shown in Fig. 4 (**a-d**) using G(+) LMMs at a 30:1 lipid/peptide molar ratio. As shown, there was little change in secondary structure for either AMP between 10 minutes and 4 days after mixing, except for a slight increase in helical content in KT9 at 4 days post mixing, which may have been within the error of the measurement.

In Fig. 3 (**a-d**) and Fig. 4 (**a,b**) a broad band at ~ 230 nm due to tryptophan excitonic coupling (Hackney et al. 2026) has been subtracted out in order to carry out the L-M fitting with the four secondary structure motifs. Fig. S2 in Online Resource shows this band in the raw data of **a)** G(-) LMM and **b)** G(+) LMM, but not in **c)** Euk33 LMM.

Low-angle and wide-angle X-ray scattering

Low-angle X-ray scattering (LAXS) yields the bending modulus, K_C, which is a measure of membrane rigidity. Wide-angle X-ray scattering (WAXS) from the same sample also determines the degree of lipid chain order, S_{xray}. Examples of the 2D X-ray images that are used to obtain K_C and S_{xray} are shown in Fig. S3 and S4, respectively, in Online Resource. Figure 5 shows that there was a gradual decrease in K_C caused by both AMPs in G(-) (**a**), G(+) (**b**) and Euk33 (**c**) LMMs, indicating that both AMPs are capable of softening these lipid model membranes, but no dramatic differences in material properties between the AMPs are observed. In G(-) (**d**) and G(+) (**e**) LMMs, both AMPs caused a small increase in lipid chain order at low concentration, and then a decrease in chain order, consistent with the changes in membrane softening. In Euk33 LMM (**f**), KT9 caused a decrease while RT9 caused an increase in lipid chain order. Although the overall Euk33 was not stiffened by RT9, the increase in lipid chain order may have contributed to its greater toxicity. Figure 5g,h show almost no change in the interchain d-spacing as either KT9 or RT9 concentration is increased in G(-) or G(+) LMMs. In Euk33, an increase in d-spacing is observed **(i**), especially for RT9 as peptide is added.

From the same samples that yield material properties and lipid chain order, structural information is obtained by using the form factors shown in Fig. S5 in Online Resource to construct electron density profiles (EDPs) as shown in Fig. 6: G(-) column **a**, G(+) column **b**, and Euk33 column **c**. The EDPs consist of the total profile (black trace) with a high peak due to the contributions from the phosphate and carbonyl groups in the headgroup. The area/lipid is calculated using the scattering density program (SDP) with V_{CH2}/D_C, which is the volume of the hydrocarbon region divided by its thickness. These structural parameters are summarized in Table 1. The AMP locations in these LMM bilayers were determined for 100:1 lipid/peptide molar ratio (G(-) and G(+)) and 50:1 for Euk33. As shown in Fig. 6, column **a,b**, KT9 located in the headgroup in both G(-) and G(+) LMMs, while RT9 was located in the

hydrocarbon interior, close to the center of the bilayer. This differential location could be related to the greater effectivity of KT9 compared to RT9 at killing bacteria. For Euk33 in Fig. 6 column c, both AMPs were embedded in the hydrocarbon interior. As shown in Table 1, KT9 decreased the area/lipid to a slightly greater extent than did RT9 in G(-) and G(+) LMMs, while RT9 increased the area/lipid slightly more than KT9 in Euk33 LMM.

Table 1
Summary of structural parameters

Sample (lipid/peptide)	**Area/lipid A_L (Å^2) (± 1.5)**	**$2D_C$ (Å) (± 0.5)**
G(-) Control	71	26.4
G(-)/KT9 (100:1)	61	30.8
G(-)/RT9 (100:1)	62	31.0
G(+) Control	72	26.4
G(+)/KT9 (100:1)	63	30
G(+)/RT9 (100:1)	66	29.6
Euk33 Control	60	35.5
Euk33/KT9 (50:1)	64	34.6
Euk33/RT9 (50:1)	66	36.5

Small-angle X-ray scattering

When we prepared samples for CD spectroscopy, we observed that the solutions became cloudy when AMP was added to ULVs, indicating the formation of structures that scatter light more strongly. An effort was made to quantitate this conversion using small-angle X-ray scattering (SAXS). Figure 7 shows results with G(-) LMMs (**a-g**), with G(+) LMMs (**h-n**) and Euk33 LMMs (**o-u**). Panels (**a, h, o**) show 2D images of ULVs before addition of AMP, panels (**b, i, p**) show ULVs with KT9 added, and panels (**c, j, q**) show ULVs with RT9 added. Azimuthal averages of the 2D images were performed and are shown below the 2D images. By scaling the pure ULV data to the ULV data in the total image, a subtraction is then carried out to determine the amount of conversion of ULV to MLV by integrating areas under the curves. The sharp, lamellar orders indicate ULV to MLV conversion with percentages summarized in Table 2.

Remarkably, as shown in Table 2, percent conversion of ULV to MLV correlated very well with bacterial killing efficacy for G(-) and G(+) LMMs, where KT9 was more efficient at ULV to MLV conversion and also at killing bacteria. In addition, RT9 was more efficient at ULV to MLV conversion in Euk33 LMMs and also more toxic to red blood cells.

Table 2
ULV to MLV conversion vs MICs

LMM/AMP	% Conversion (ULV to MLV)	MIC (μM)
G(-)/KT9	18.5 ± 1.0	3.8 ± 2.7
G(-)/RT9	11.9 ± 1.7	7.0 ± 6.1
G(+)/KT9	33.3 ± 2.5	2.5 ± 1.6
G(+)/RT9	12.2 ± 0.3	6.4 ± 3.7
		% Toxicity (32 μM)
Euk33/KT9	7.6 ± 0.4	15
Euk33/RT9	37.7 ± 2.5	39

Discussion

This work compares two novel 18-mer AMPs, named RT9 and KT9, since they each contain 9 cationic amino acid residues. Of the remaining 9 AA's, four are tryptophan (W) which are positioned near the interface between hydrophobic and cationic residues in a helical wheel diagram (Fig. 1), and the remainder are valine. Previously, we found that similar AMPs with four W's produced the lowest MICs near 18 AA's length (Xiang et al. 2022). The purpose of the present study was to find correlations between biophysical properties such as bilayer membrane rigidity, lipid chain order, bilayer structure and peptide secondary structure with bacterial killing efficacy and toxicity. In this work, secondary structures were nearly identical (Figs. 3,4) for all three LMMs, with random coil and beta-sheet the dominant structural motifs, with little helical content. Other investigations have found that helix and beta-sheet peptides are frequently found to be effective AMPs, but that even the random coil structure can be effective, such as in indolicin (Yang et al. 2025). In all three LMMs, both AMPs caused a membrane softening, which did not distinguish their behaviors. In Euk33 LMMs, RT9 caused an increase in lipid chain order compared to KT9; this increased chain ordering could be related to the increased toxicity of RT9 to red blood cells, by disrupting a fluid-phase bilayer, causing leakage. As for structural differences, the headgroup location of KT9 may be related to its superior ability to interact with both G(-) and G(+) bacteria, compared to the hydrophobic location of RT9 in G(-) and G(+) LMMs. In the Euk33 LMM, both AMPs were located in the hydrocarbon interior, suggesting that even the small toxicity of KT9 is correlated with this location in these neutral LMMs, causing a perturbation of the lipid chain region.

The most dramatic difference between RT9 and KT9, however, was their differential ability to cause fusion of unilamellar vesicles into multilamellar vesicles. The fusion event, as evidenced by SAXS to quantitate the formation of MLVs from ULVs, is a measure of membrane destabilization. While many investigators have purported that bacterial killing efficacy by AMPs is primarily associated with a non-specific breach of the bacterial membrane, there are intracellular events that could be equally, or more

important. These include binding to DNA, associating with the ribosome, disrupting ATP homeostasis, cell wall biosynthesis and other central metabolic pathways, as well as producing reactive oxygen species (Ajayi et al. 2025; Canales et al. 2026). In fact, some investigators claim that AMPs are actually cell penetrating peptides (CPPs) that act as a moving van into a cell, entering only to “deliver” various bioactive molecules, rather than disrupting the membrane (Gori et al. 2023). Previous studies have shown that arginine-rich CPPs are more effective at penetrating membranes (Ciobanasu et al. 2010), but that lysine-rich peptides are more effective at membrane destabilization (Rodrigues et al. 2024). The results of the present study are similar to our recently published comparison of another pair of R vs. K AMPs, W6K8 vs. W6R8 (Hackney et al. 2026), where we also found that the K form of AMP was more successful at killing bacteria and also caused more ULV-to-MLV conversion (membrane destabilization). Therefore, we suggest that membrane destabilization is a necessary step in bacterial killing and also in eukaryotic membrane lysis. This raises the question as to why the K-form of the AMP is more effective in destabilizing bacterial LMMs, but that the R form is more effective at destabilizing eukaryotic LMMs. As we discussed in (Hackney et al. 2026), the interaction of the cation (R or K) with the delocalized conjugated Pi electrons of the indole ring of W is more stable between W and R than between W and K (Gallivan and Dougherty 1999). This could liberate K to interact more strongly with negatively charged groups in the bacterial LMMs, which could be the reason that KT9 locates in the headgroup region. For the Euk33 LMMs, the R-W cation-Pi complex may be able to destabilize these neutral membranes to a larger degree than K or W alone. Subsequently, intracellular targets may also be compromised but that was not studied here.

Conclusion

This study systematically used circular dichroism, x-ray diffuse scattering and small angle x-ray scattering as biophysical tools to characterize the interaction between RT9 and KT9 with three different lipid model membranes (LMMs) mimicking Gram-negative and Gram-positive bacterial membranes and eukaryotic membranes. Both AMPs softened all three LMMs, but only RT9 increased lipid chain order in Euk33 LMMs. Both AMPs decreased the area/lipid in both bacterial LMMs, and increased the area/lipid in Euk33 LMMs, but there were only small differences between the AMPs’ effects. The location of KT9 was in the headgroup region for G(-) and G(+) LMMs, while RT9 was in the hydrocarbon region, and both AMPs were in the hydrocarbon region of Euk33 LMMs. The primary difference between the AMPs was in membrane destabilization as monitored using SAXS. The percent conversion of ULVs to MLVs was nearly twice as great for KT9 vs RT9 in bacterial LMMs, which correlated with the greater efficiency of bacterial killing of KT9. For eukaryotic LMMs, the percent conversion of ULVs to MLVs was greater for RT9 which correlated with its greater toxicity. We suggest that membrane destabilization is a necessary step for bacterial killing efficiency and for red blood cell lysis.

Declarations

Acknowledgements:

The authors acknowledge the Materials Characterization Facility at Carnegie Mellon University (MCF-677785) for facilitating the use of the Xenocs Xeuss 3.0. This work is also based upon research conducted at the Center for High Energy X-ray Sciences (CHEXS at CHESS), which is supported by the National Science Foundation under award DMR- 1829070, and the Macromolecular Diffraction at CHESS (MacCHESS) facility, which is supported by award 1-P30-GM124166-01A1 from the National Institute of General Medical Sciences, National Institutes of Health, and by New York State's Empire State Development Corporation (NYSTAR). Additional support is from the National Institute of Allergy and Infectious Diseases (NIAID) 1R01AI172861-01A1 (B.D., S.T.-N.), NASA Pennsylvania Space Grant Consortium (L.K.). The authors would also like to acknowledge Dr. Stephen Paul Meisburger for his help at CHEXS (CHESS).The authors would like to acknowledge Nathan Gaynor for helpful comments.

Author contribution statement: STN conceived, designed the research and wrote the manuscript, while LH, AL and RP helped to write the manuscript. LH, AH, AB, WG collected and analyzed CD data. AL, RP, AH, DW, WG, VY, ZH, MC, LK, JJ collected and/or analyzed LAXS or WAXS X-ray data. JK and WX carried out microbiological experiments at Pitt. BD engineered the peptides and provided funding, peptides and critical comments.

Ethical approval: No animals or humans were used in these experiments. All authors consent to publish this manuscript's contents.

Funding: The authors acknowledge the Materials Characterization Facility at Carnegie Mellon University (MCF-677785) for facilitating the use of the Xenocs Xeuss 3.0. This work is also based upon research conducted at the Center for High Energy X-ray Sciences (CHEXS at CHESS), which is supported by the National Science Foundation under award DMR- 1829070, and the Macromolecular Diffraction at CHESS (MacCHESS) facility, which is supported by award 1-P30-GM124166-01A1 from the National Institute of General Medical Sciences, National Institutes of Health, and by New York State's Empire State Development Corporation (NYSTAR). Additional support is from the National Institute of Allergy and Infectious Diseases (NIAID) 1R01AI172861-01A1 (B.D., S.T.-N.), NASA Pennsylvania Space Grant Consortium (L.K.).

Data availability: Biophysical data will be made available upon request to Stephanie Tristram-Nagle (stn@cmu.edu) and microbiological data will be made available upon request to Berthony Deslouches (tdesl19@pitt.edu).

References

1. Aisenbrey C, Marquette, A., Bechinger, B. (2019) The mechanisms of action of cationic antimicrobial peptides refined by novel concepts from biophysical investigations. In: KatsumiMatsuzaki (ed) Antimicrobial Peptides Basics for Clinical Application, Advances in Experimental Medicine and Biology vol 1117. Springer Nature Singapore, Singapore, pp 33-64

2. Ajayi OE, Bellavita R, Imbo LE, Palladino S, Braccia S, Falanga A, Galdiero S (2025) Boosting AMPs' power: From structural engineering to nanotechnology-based delivery. Molecules 30(14)'doi.org/10.3390/molecules30142979'.
3. Canales CSC, dos Santos MD, Negri ACC, Gois LR, Vishwakarma SK, Roque-Borda CA, Pavan FR (2026) Antimicrobial peptides against ESKAPE pathogens: Mechanisms, molecular optimization, and current limitations. Future Pharmacology 6(2)'doi.org/10.3390/futurepharmacol6020032'.
4. CDC (2025) Antimicrobial resistance facts and stats. Antimicrobial Resistance https://www.cdc.gov/antimicrobial-resistance/data-research/facts-stats/index.html.
5. Chen FY, Lee MT, Huang HW (2003) Evidence for membrane thinning effect as the mechanism for peptide-induced pore formation. Biophysical Journal 84(6):3751-3758 'doi.org/10.1016/S0006-3495(03)75103-0'.
6. Ciobanasu C, Siebrasse JP, Kubitscheck U (2010) Cell-penetrating HIV1 TAT peptides can generate pores in model membranes. Biophysical Journal 99(1):153-162 'doi.org/10.1016/j.bpj.2010.03.065'.
7. Deslouches B, Steckbeck JD, Craigo JK, Doi Y, Mietzner TA, Montelaro RC (2013) Rational design of engineered cationic antimicrobial peptides consisting exclusively of arginine and tryptophan, and their activity against multidrug-resistant pathogens. Antimicrobial agents and chemotherapy 57(6):2511-2521 'doi.org/10.1128/aac.02218-12'.
8. Epand RM, Epand RF (2009) Lipid domains in bacterial membranes and the action of antimicrobial agents. Biochimica et Biophysica Acta (BBA)-Biomembranes 1788(1):289-294 'doi.org/10.1016/j.bbamem.2008.08.023'.
9. Gallivan JP, Dougherty DA (1999) Cation-π interactions in structural biology. Proceedings of the National Academy of Sciences of the United States of America 96(17):9459-9464 'doi.org/10.1073/pnas.96.17.9459'.
10. Gori A, Lodigiani G, Colombarolli SG, Bergamaschi G, Vitali A (2023) Cell penetrating peptides: Classification, mechanisms, methods of study, and applications. ChemMedChem 18(17):e202300236 'doi.org/10.1002/cmdc.202300236'.
11. Hackney A, Hartmann L, Parasnis R, Leong A, Chen MT, Knox L, Jaber J, Gao WC, Dupuy F, Xiang WY, Klousnitzer J, Deslouches B, Tristram-Nagle S (2026) Lysine is more effective than arginine in two tryptophan-rich antimicrobial peptides. Biochimica Et Biophysica Acta-Biomembranes 1868(4)'doi.org/10.1016/j.bbamem.2026.184548'.
12. Hale JD, Hancock RE (2007) Alternative mechanisms of action of cationic antimicrobial peptides on bacteria. Expert Review of Anti-Infective Therapy 5(6):951-959 'doi.org/10.1586/14787210.5.6.951'.
13. Hallock KJ, Lee DK, Ramamoorthy A (2003) MSI-78, an analogue of the magainin antimicrobial peptides, disrupts lipid bilayer structure via positive curvature strain. Biophysical Journal 84(5):3052-3060 'doi.org/10.1016/S0006-3495(03)70031-9'.
14. He K, Ludtke SJ, Worcester DL, Huang HW (1996) Neutron scattering in the plane of membranes: Structure of alamethicin pores. Biophysical Journal 70(6):2659-2666 'doi.org/10.1016/S0006-3495(96)79835-1'.

15. Heinrich F, Salyapongse A, Kumagai A, Dupuy FG, Shukla K, Penk A, Huster D, Ernst RK, Pavlova A, Gumbart JC, Deslouches B, Di YP, Tristram-Nagle S (2020) Synergistic biophysical techniques reveal structural mechanisms of engineered cationic antimicrobial peptides in lipid model membranes. Chemistry-a European Journal 26(28):6247-6256 'doi.org/10.1002/chem.202000212'.
16. Kučerka N, Nagle JF, Sachs JN, Feller SE, Pencer J, Jackson A, Katsaras J (2008) Lipid bilayer structure determined by the simultaneous analysis of neutron and x-ray scattering data. Biophysical Journal 95(5):2356-2367 'doi.org/10.1529/biophysj.108.132662'.
17. Liu YF, Nagle JF (2004) Diffuse scattering provides material parameters and electron density profiles of biomembranes - art. no. 040901. Physical Review E 69(4)'doi.org/10.1103/PhysRevE.69.040901'.
18. Lyatskaya Y, Liu Y, Tristram-Nagle S, Katsaras J, Nagle JF (2000) Method for obtaining structure and interactions from oriented lipid bilayers. Physical Review E 63(1):011907 'doi.org/10.1103/PhysRevE.63.011907'.
19. Matsuzaki K, Sugishita K-i, Harada M, Fujii N, Miyajima K (1997) Interactions of an antimicrobial peptide, magainin 2, with outer and inner membranes of Gram-negative bacteria. Biochimica et Biophysica Acta (BBA)-Biomembranes 1327(1):119-130 'doi.org/10.1016/S0005-2736(97)00051-5'.
20. Mills TT, Toombes GE, Tristram-Nagle S, Smilgies D-M, Feigenson GW, Nagle JF (2008) Order parameters and areas in fluid-phase oriented lipid membranes using wide angle X-ray scattering. Biophysical journal 95(2):669-681 'doi.org/10.1529/biophysj.107.127845'.
21. Mitra S, Coopershlyak M, Li Y, Chandersekhar B, Koenig R, Chen M-T, Evans B, Heinrich F, Deslouches B, Tristram-Nagle S (2023) Novel helical Trp-and Arg-rich antimicrobial peptides locate near membrane surfaces and rigidify lipid model membranes. Advanced NanoBiomed Research 3:2300013 'doi.org/10.1002/anbr.202300013'.
22. Rathinakumar R, Wimley WC (2008) Biomolecular engineering by combinatorial design and high-throughput screening: Small, soluble peptides that permeabilize membranes. Journal of the American Chemical Society 130(30):9849-9858 'doi.org/10.1021/ja8017863'.
23. Rodrigues FEP, Darbre T, Machuqueiro M (2024) High charge density in peptide dendrimers is required to destabilize membranes: Insights into endosome evasion. Journal of Chemical Information and Modeling 64(8):3430-3442 'doi.org/10.1021/acs.jcim.4c00018'.
24. Shai Y (1999) Mechanism of the binding, insertion and destabilization of phospholipid bilayer membranes by α-helical antimicrobial and cell non-selective membrane-lytic peptides. Biochimica et Biophysica Acta (BBA)-Biomembranes 1462(1-2):55-70 'doi.org/10.1016/S0005-2736(99)00200-X'.
25. Tristram-Nagle SA (2007) Preparation of oriented, fully hydrated lipid samples for structure determination using X-ray scattering. Methods Mol Biol 400:63-75 'doi.org/10.1007/978-1-59745-519-0_5'.
26. Wu GQ, Wu HB, Li LX, Fan XB, Ding JX, Li XF, Xi T, Shen ZL (2010) Membrane aggregation and perturbation induced by antimicrobial peptide of S-thanatin. Biochemical and Biophysical Research Communications 395(1):31-35 'doi.org/10.1016/j.bbrc.2010.03.107'.

27. Xiang W, Clemenza P, Klousnitzer J, Chen J, Qin W, Tristram-Nagle S, Doi Y, Di YP, Deslouches B (2022) Rational framework for the design of Trp-and Arg-rich peptide antibiotics against multidrug-resistant bacteria. Frontiers in microbiology 15:889791 'doi.org/10.3389/fmicb.2022.889791'
28. Yang R, Ma XH, Peng F, Wen J, Allahou LW, Williams GR, Knowles JC, Poma A (2025) Advances in antimicrobial peptides: From mechanistic insights to chemical modifications. Biotechnology Advances 81: 108570 'doi.org/10.1016/j.biotechadv.2025.108570'.
29. Zhang RT, Suter RM, Nagle JF (1994) Theory of the structure factor of lipid bilayers. Physical Review E 50(6):5047-5060 'doi.org/10.1103/PhysRevE.50.5047'.

Figures

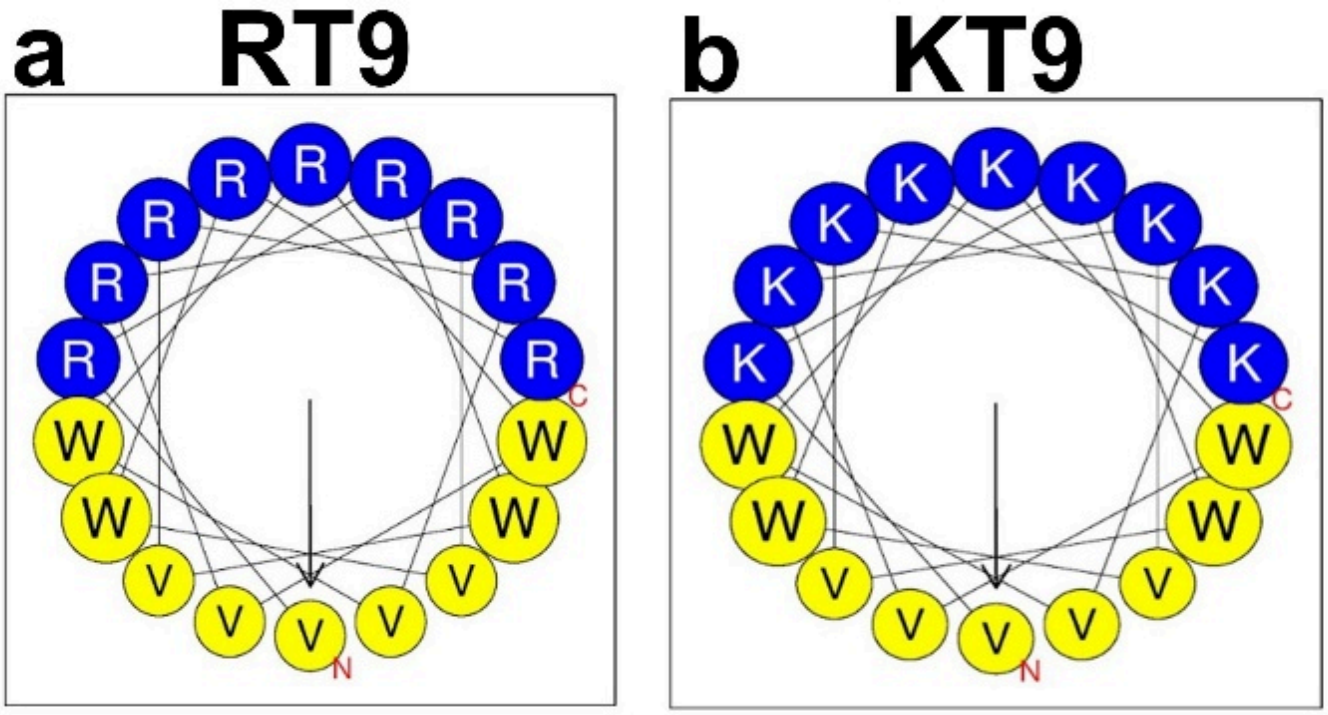


Figure 1

Helical wheel representations of **a**) **RT9** (VR RW VR RV WR WV RR VW RR) and **b**) **KT9** (VK KW VK KV WK WV KK VW KK). The arrows show direction and magnitude of hydrophobic moment.

a

AMP	G(+)		Average MIC (μM)			G(-)
	EF	**SA**	**KP**	**AB**	**PA**	**EC**
RT9	9 ± 8.4	3.7 ± 3.8	5.0 ± 2.0	1.9 ± 1.4	15.9 ± 12.4	5.0 ± 2.0
KT9	1.3 ± 0.8	3.6 ± 4.0	3.6 ± 1.0	1.0 ± 0.3	7.4 ± 6.6	3.1 ± 1.2

b

AMP	% RBC Lysis	
	16 μM	**32 μM**
RT9	35	39
KT9	8	15

Figure 2

a) Average MIC values of G(+) (pink fill) and G(-) (yellow fill) bacteria. Abbreviations: EF, *Enterococcus faecalis* SA, *Staphylococcus aureus* KP, *Klebsiella pneumoniae* AB, *Acinetobacter baumannii*PA, *Pseudomonas aeruginosa* EC, *Escherichia coli* **b)** Percent red blood cell lysis

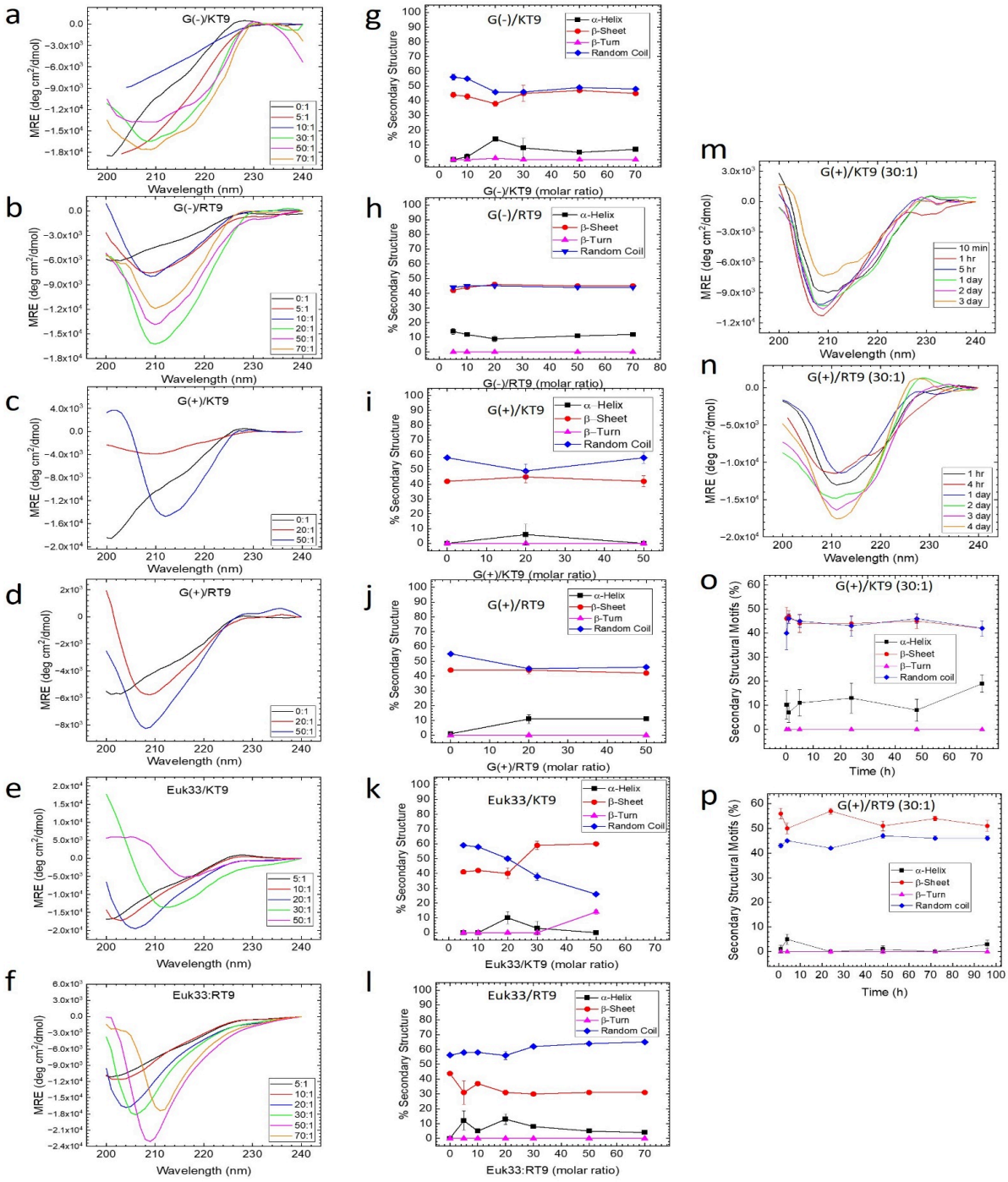


Figure 3

MREs of KT9 and RT9 in G(-) LMM (**a,b**), G(+) LMM (**c,d**), Euk33 LMM (**e,f**). Percent composition secondary structure of KT9 and RT9 in G(-) LMM (**g,h**), G(+) LMM (**i,j**), Euk33 LMM (**k,l**)

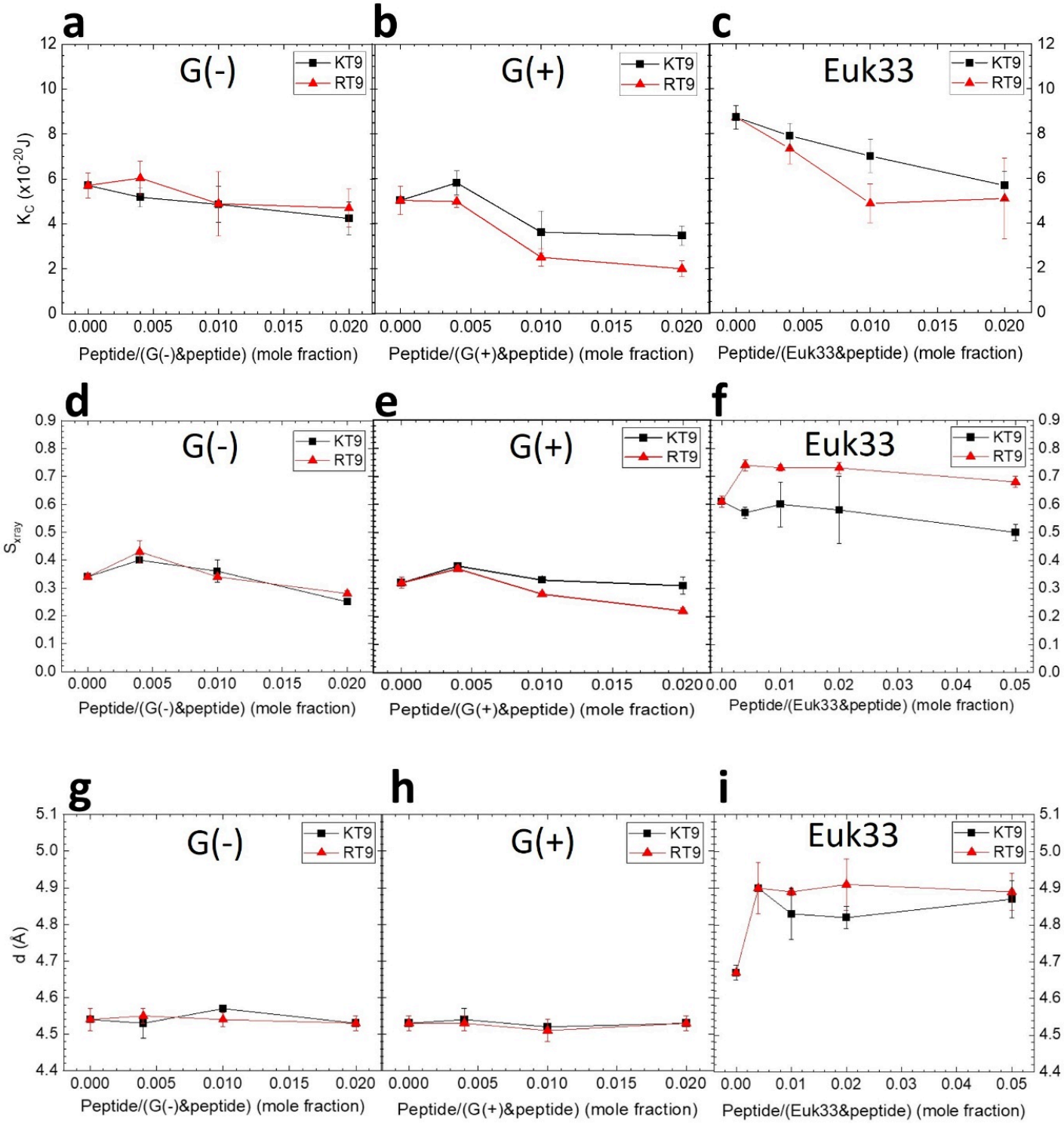


Figure 4

Bending modulus (K_C) vs. peptide/(peptide&lipid) (mole fraction), **a**) G(-), **b**) G(+), **c**) Euk33 LMM. Lipid chain order parameter (S_{xray}) vs. peptide/(peptide&lipid) (mole fraction), **d**) G(-), **e**) G(+), **f**) Euk33 LMM. Inter-chain d-spacing vs. peptide/(peptide&lipid) (mole fraction), **g**) G(-), **h**) G(+), **i**) Euk33 LMM

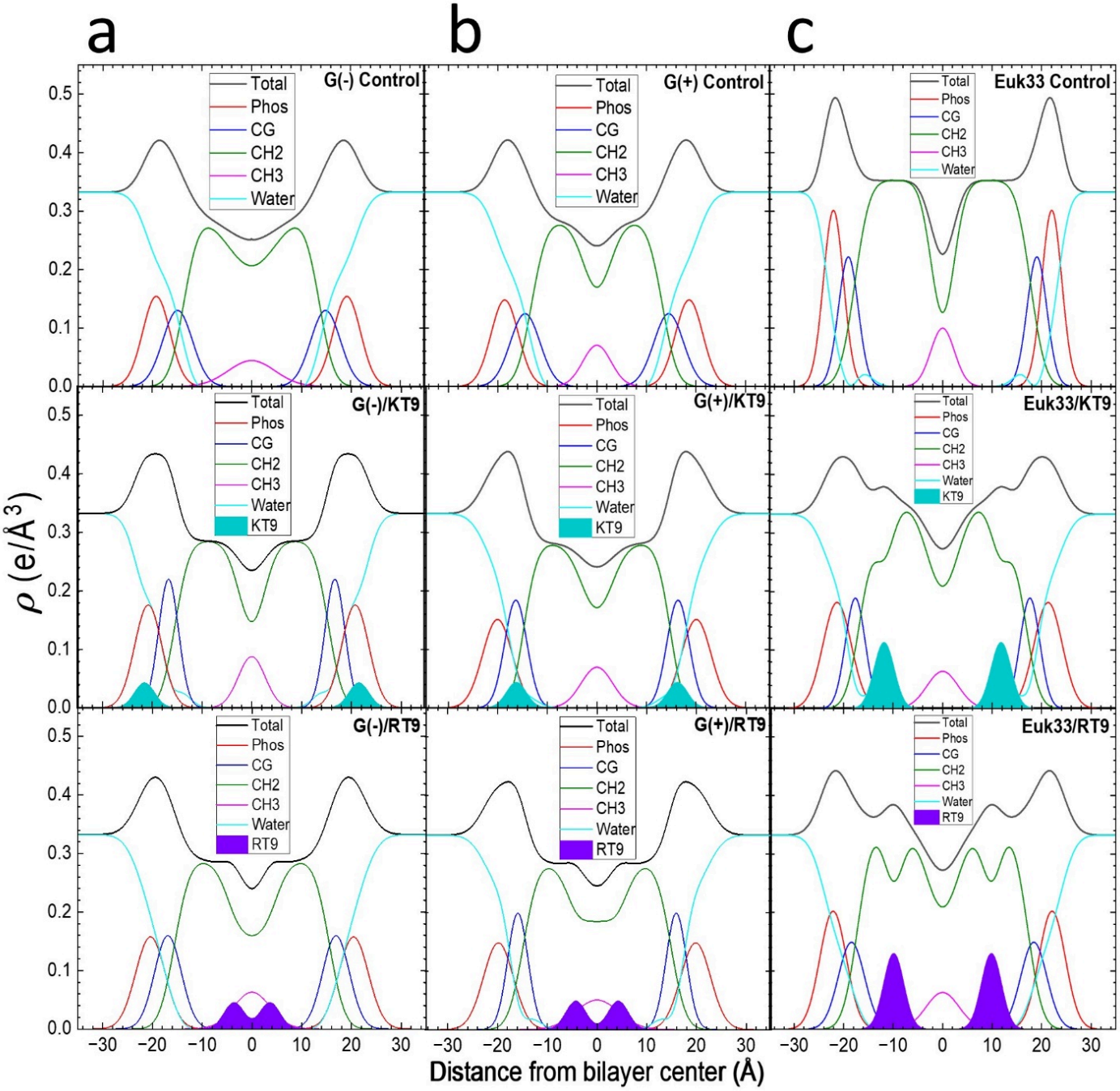


Figure 5

Electron density profiles (EDPs) showing bilayer component groups: Total (black), phosphate and outer headgroup, Phos (red), carbonyl glycerol, CG (blue), chain methylenes, CH2 (green), terminal methyl groups, CH3 (magenta), water (cyan) and AMP, filled Gaussians, KT9 (cyan) and RT9 (purple). Column **a**) G(-) LMM, **b**) G(+) LMM and **c**) Euk33 LMM.

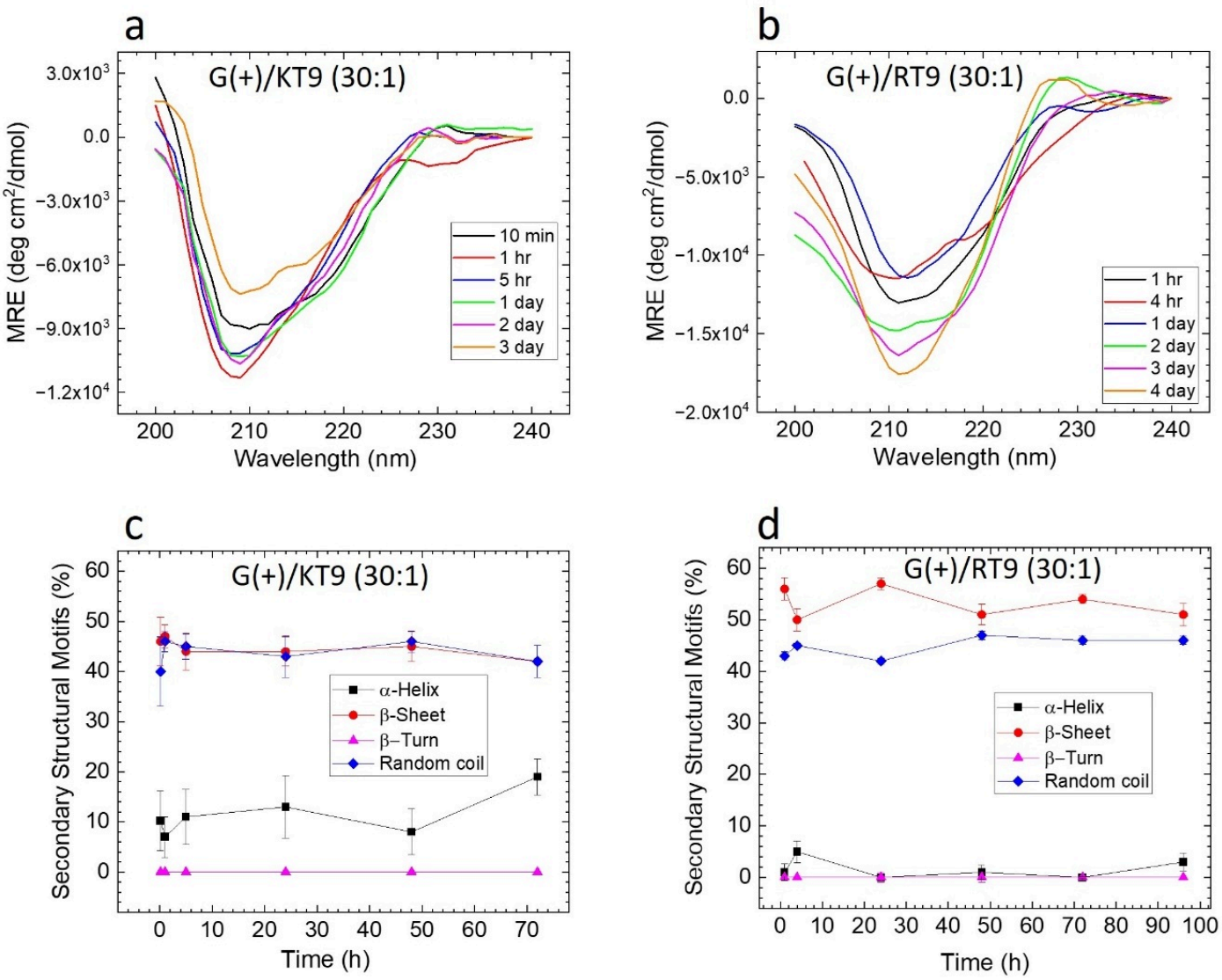


Figure 6

Kinetics of formation of secondary structure of KT9 and RT9 in G(+) LMM (30:1 lipid/peptide molar ratio) at 37 oC, MREs (**a,b**), Percent composition (**c,d**)

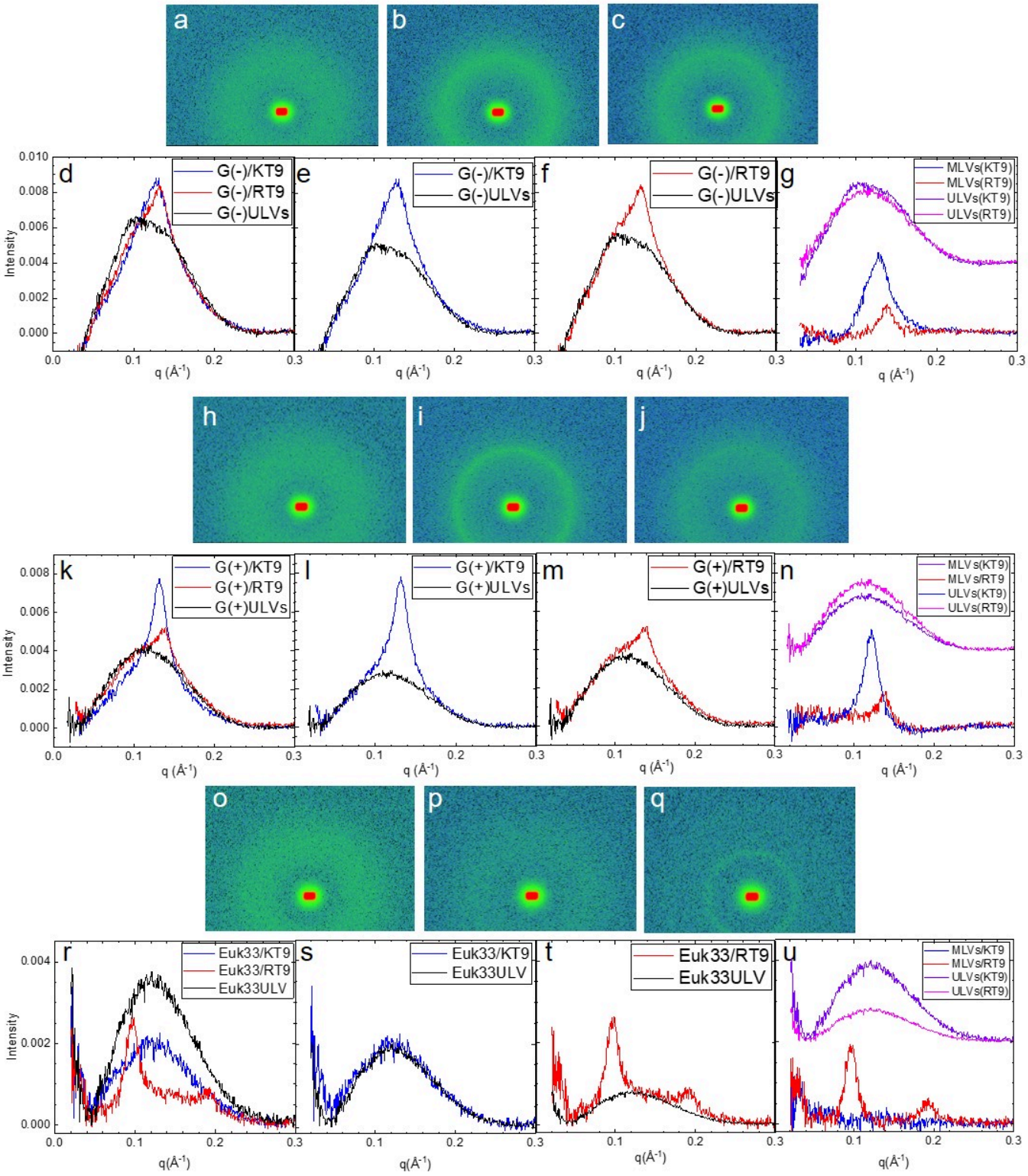


Figure 7

2D SAXS data at 37 °C. G(-) LMM (**a-c**), G(+) LMM (**h-j**), Euk33 LMM (**o-q**) with KT9 (b**, i, p**) or RT9 (**c, j, q**). 1D azimuthal averages of 2D data: raw data (**d, k, r**), KT9 with scaled ULV **(e, l, s**), RT9 with scaled ULV **(f, m, t**), total samples minus scaled ULV for G(-) (**g**), G(+) (**n**) and Euk33 (**u**). All samples had buffer subtracted before plotting and analysis. Standard deviations arise from multiple fittings to the same data.

Supplementary Files

This is a list of supplementary files associated with this preprint. Click to download.

- T9SISTN.pdf